This document is published in:

Physics in Medicine and Biology, Vol. 59, nº 2 (2014), pp. 421-439

DOI: http://dx.doi.org/10.1088/0031-9155/59/2/421

Dual-exposure technique for extending the dynamic range of x-ray flat panel detectors

A Sisniega[1,2], M Abella[1,2], M Desco[1,2,3] and J J Vaquero[1,2]

[1] Departamento de Bioingeniería e Ingeniería Aeroespacial, Universidad Carlos III de Madrid, Madrid, Spain
[2] Instituto de Investigación Sanitaria Gregorio Marañón (IiSGM), Madrid, Spain
[3] Centro de Investigación en Red de Salud Mental (CIBERSAM), Madrid, Spain

E-mail: juanjose.vaquero@uc3m.es

Abstract

This work presents an approach to extend the dynamic range of x-ray fla panel detectors by combining two acquisitions of the same sample taken with two different x-ray photon flu levels and the same beam spectral configuration In order to combine both datasets, the response of detector pixels was modelled in terms of mean and variance using a linear model. The model was extended to take into account the effect of pixel saturation. We estimated a joint probability density function (j-pdf) of the pixel values by assuming that each dataset follows an independent Gaussian distribution. This j-pdf was used for estimating the fina pixel value of the high-dynamic-range dataset using a maximum likelihood method. The suitability of the pixel model for the representation of the detector signal was assessed using experimental data from a small-animal cone-beam micro-CT scanner equipped with a fla panel detector. The potential extension in dynamic range offered by our method was investigated for generic fla panel detectors using analytical expressions and simulations. The performance of the proposed dual-exposure approach in realistic imaging environments was compared with that of a regular single-exposure technique using experimental data from two different phantoms. Image quality was assessed in terms of signal-to-noise ratio, contrast, and analysis of profile drawn on the images. The dynamic range, measured as the ratio between the exposure for saturation and the exposure equivalent to instrumentation noise, was increased from 76.9 to 166.7 when using our method. Dual-exposure results showed higher contrast-to-noise ratio and contrast resolution than the single-exposure acquisitions for the same x-ray dose. In addition, image artifacts were reduced in the combined dataset. This technique to extend the dynamic range of the detector without

increasing the dose is particularly suited to image samples that contain both low and high attenuation regions.

1. Introduction

The use of digital detectors for the acquisition of x-ray imaging is becoming commonplace in the clinical and preclinical practice (Kalender and Kyriakou 2007). Flat panel indirect (FP) detectors are becoming the most common choice, either for two-dimensional (2D) radiographic digital imaging or for cone-beam CT (CBCT). FP based x-ray systems are used nowadays in a variety of scenarios, such as digital radiography (Korner *et al* 2007), C-arm systems, for interventional fluorosco y (Siewerdsen *et al* 2007) or CBCT (Siewerdsen *et al* 2005), musculoskeletal CBCT imaging (Zbijewski *et al* 2011), kVp CBCT systems coupled to linear accelerators for image guided radiation therapy (Jaffray *et al* 2002), breast CBCT systems (Boone *et al* 2001), or small-animal micro-CT (CBμCT) imaging (Badea *et al* 2008, Vaquero *et al* 2008).

However, the limited dynamic range (DR) of FP detectors could compromise image quality when a sample has both low- and high-density materials. DR values are commonly measured as the ratio of saturation charge to the noise floo . Typical values, as reported by the manufacturers, may be 2000 for a Hamamatsu C7940DK-02 (Hamamatsu Photonics k. k., Hamamatsu, Japan) or 4000 for the Shad-o-Box (Rad-icon Imaging Corp, Santa Clara, CA).

The consequence of this limited DR is that dense areas may become obscured in 2D imaging if the exposure is adjusted to better observe the anatomy of soft tissues. This issue is of greater importance in CBCT because commonly used analytical reconstruction algorithms, such as FDK (Feldkamp *et al* 1984), produce severe artifacts in the reconstructed slices when the fiel of view (FOV) covered by the acquired projections truncates the object under examination (Feldkamp *et al* 1984, Yu *et al* 2006). Thus, the scanner FOV should be larger than the size of the sample. If the subject has a high attenuation region, it is not possible to obtain sufficien signal-to-noise ratio (SNR) inside this area without saturating the detector elements in the object-free region. Such a problem can arise in any CT scanner, when the DR of the subject exceeds that of the detector.

Several approaches have been proposed to address this issue. Most of them were originally developed for optical imaging (i.e. photography and video) and are based on hardware modification or special detector designs. Some implementations include the use of a non-conventional pixel design (Lule *et al* 1999), multiple sensors inside a single pixel (Fox *et al* 2005), spatially varying pixel sensitivity (Nayar and Mitsunaga 2000), or combinations of special scintillator and pixel designs (Nittoh *et al* 2003). In addition to these approaches, a small number of software-based methods have been proposed. An example can be found in Clinthorne and Strobel (1998), who mathematically estimated a high dynamic range (HDR) dataset from the low DR image.

Some of the most widely used software-based techniques for extending the DR of optical image detectors (e.g. for photography and video) are based on the acquisition of several images, each with a different exposure to incident radiation (Mann and Picard 1995). The acquired data are then combined to obtain a new HDR image. The combination algorithm to obtain the value of a pixel of the HDR image can be as simple as the selection of the best sample from

the two original datasets (Madden 1993), or a more elaborate process, which takes advantage of all the information contained in the acquired data (Dromigny and Zhu 1997, Robertson *et al* 2003).

The use of multi-exposure-based techniques to extend the DR of FP detectors in CBμCT has been reported previously. Sukovic and Clinthorne (2001) proposed an approach to increase the DR of projection data by combining two datasets acquired with different exposure (mAs). However the DR of the resulting data was not compared with that achieved by conventional scanning methods, and discontinuities were noticeable in the HDR data.

We introduce a novel dual-exposure technique to extend the DR of FP detectors. The method combines two projection datasets using a maximum likelihood estimation based on previous knowledge of the detector response to incoming radiation. The detector response is described using an analytical model (Yang *et al* 2010) for pixel mean and variance, which was extended to include the effect of saturation. We obtained the model parameters for a real detector, and the validity of this model was assessed using experimental data. The performance of our method to extend the DR and its potential limits were evaluated using simulated data and realistic imaging scenarios with experimental 2D projection images and CBCT data from a commercial CBμCT scanner.

2. Material and methods

In the following sections we introduce the theoretical basis of our DR extension method, describing the modifie acquisition and mathematical processing of the data. To this end, we present a detector pixel model (section 2.1.1) that provides an estimation of the pixel signal and variance as a function of the exposure, and constitutes the basis for the subsequent maximum likelihood estimation of the HDR data (section 2.1.2).

In section 2.2 we describe how to obtain a parametric description of the detector pixel model from experimental data acquired with a real FP detector, and evaluate the agreement between the pixel model and detector experimental data.

The set of parameters is then employed for the theoretical evaluation of the DR extension capability in ideal environments, as explained in section 2.3.1. The method is finall evaluated with experimental data in sections 2.3.2 (for 2D projection data) and 2.3.3 (for 3D tomographic data).

2.1. Generation of HDR projection data

The aim of our method is to obtain x-ray projection data with a DR larger than that showed by the detector using a regular acquisition protocol.

In order to generate the HDR data, two datasets are acquired at two x-ray exposure levels (for the same kVp and beam filtration) First, a data acquisition is performed using an exposure value that guarantees that no pixel in the detector is saturated, followed by the acquisition of a partially saturated dataset.

Figure 1 outlines the workfl w of the HDR data generation process. The following subsections detail the different steps.

For the exposure used in the firs scan, very high attenuation regions of the object may be underexposed, not providing a valid signal.

The second scan is carried out at a higher anode current, which makes it possible to obtain a partially saturated dataset that provides improved information about all or, at least, some of the underexposed areas of the firs scan. The ratio of the current for the second acquisition to that of the firs one (i.e., the Bucky factor for the second acquisition) is denoted as A_2.

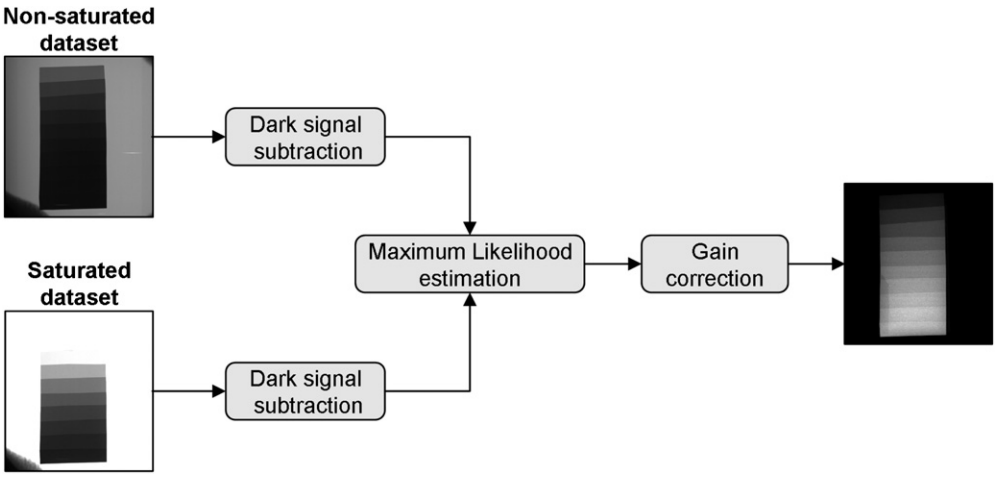

Figure 1. Outline of the dual-exposure method to obtain an HDR projection. Two datasets are acquired at different x-ray flu levels, and the dark signal is subtracted from both of them. Both datasets are combined using a maximum likelihood approach to generate the HDR data, which eventually undergo a standard gain correction step.

Both datasets are then combined following the method described below, which is based on a previous proposal by Robertson *et al* (2003), modifie to meet the particular features of x-ray FP detectors. In particular, our method uses the concept of maximum likelihood estimation introduced by Robertson but including realistic models for the FP detector pixel signal and its variance.

2.1.1. Pixel model. To build the pixel model we assume that FP detectors show a linear relationship between the exposure and pixel signal and that the statistics of the incoming photons follow a compound Poisson model (Whiting *et al* 2006), for which a linear relationship between variance and mean still holds. We defin a simple linear model for the pixel mean response (m) and its variance (v), following Yang *et al* (2010), but introducing the concept of instrumentation noise equivalent exposure (INEE), as define in Yadava *et al* (2008):

$$m(X) = gX + p, \tag{1a}$$

$$v(X) = hg[X + X_n], \tag{1b}$$

where X is the exposure at the detector surface, g is the linear gain factor of the pixel, p is the mean dark offset of the pixel (i.e., the mean pixel signal in the absence of radiation), h is the linear factor relating mean and variance of the pixel signal, and X_n is the INEE.

X_n corresponds to the exposure value for which the quantum and instrumentation noise sources contribute equally to the total noise (Yadava *et al* 2008) or, analogously, to the minimum exposure for which the performance of the detector is still limited by image quanta.

X_n accounts for all sources of instrumentation noise (such as thermal noise, amplifie read-out noise or quantization noise) and can be easily measured (Yadava *et al* 2008) without knowing the individual noise components.

This simple model does not take into account the pixel saturation that arises for large values of X. We propose to extend the model by modifying equation (1*b*) to include the clipping introduced by saturation. The detailed derivation of the value of $v(X)$ including the effect of saturation is explained in the appendix.

2.1.2. Joint probability density function and maximum likelihood estimation. To combine the datasets obtained at two different exposures we define a joint probability density function (j-pdf) for the acquired data.

According to the previously described pixel model, each pixel observation can be considered a realization of a Gaussian-distributed random variable (Whiting *et al* 2006), with mean and variance given by equations (1*a*) and (1*b*) if the signal lies inside the non-saturated range.

Since values of a single pixel in both datasets are independent realizations of two Gaussian variables, the j-pdf of the multi-exposure data can be expressed as the product of the pdfs of N ($N = 2$) random variables, yielding

$$P(\mathbf{Y_j}) \propto \exp\left(-\sum_{i}^{N} \frac{(Y_{ij} - m(A_i X_j))^2}{v(A_i X_j)}\right) \tag{2}$$

where Y_{ij} is the recorded pixel value for pixel j and acquisition i and $\mathbf{Y_j}$ is the vector of the N values recorded for pixel j, and A_i is the ratio between exposure for the ith acquisition and the exposure for the firs acquisition. Although the formula is general for N acquisitions, in our implementation we have only combined two datasets.

The HDR signal for pixel j is estimated as the value of gX_j that maximizes the probability of observation of the acquired data or, equivalently, minimizes the absolute value of the exponent in equation (2), yielding the following expression for the objective function:

$$O(gX_j) = \sum_{i}^{N} \frac{(Y_{ij} - m(A_i gX_j))^2}{v(A_i gX_j)}. \tag{3}$$

Equation (3) can be minimized by iterative approximations, but the proposed method is aimed at the raw data processing stage, which is usually highly demanding in terms of processing time. For this reason, we propose to replace the gX_j term in the denominator by the actual pixel value after dark correction ($Y_{ij} - p_j$). Deriving equation (3) with respect to gX_j after performing the approximation in the denominator and leaving the resulting equation equal to zero, the expression for the maximum likelihood estimation of gX_j becomes:

$$gX_j = \frac{\sum_i^N \frac{A_i(Y_{ij} - p_j)}{h(Y_{ij} - p_j) + n}}{\sum_i^N \frac{A_i^2}{h(Y_{ij} - p_j) + n}} \tag{4}$$

where n is the instrumentation noise of the system, given by, $n = hgX_n$.

To ensure that the signal will be valid over a continuous range, A values must be properly selected to ensure some degree of overlap between the gain curves of the acquisitions, i.e., pixels below the DR of the detector in the ith acquisition must not be saturated in the $(i + 1)$th acquisition.

2.2. Experimental setup and data analysis for the detector model

We validated the analytical model for the detector and the HDR extension method using a commercial small-animal multimodality imaging system, the Argus PET/CT (Sedecal, Madrid, Spain). To assess the validity of the model, we acquired image data for several exposure levels and fitte the measured parameters to the detector model. Using the acquired data, we obtained a set of parameter values (g, h, p, and X_n, as described in section 2.1.1) that characterize the response of the detector for a configuratio suitable for small-animal imaging scenarios.

2.2.1. CBμCT system description and exposure estimation. The CBμCT subsystem of the Argus PET/CT is a small-animal CT designed to provide anatomical information to complement functional PET data. A thorough description and evaluation of the system can be found in Vaquero *et al* (2008).

The system incorporates a microfocus x-ray source (Oxford Instruments plc, Oxfordshire, UK) based on a tungsten anode with maximum peak energy of 50 kVp and a maximum continuous power of 50 W (anode current range 0–1 mA). The x-ray beam is filtere with 1 mm Al, which adds to the 0.125 mm thick Be output window.

The x-ray detector is a CMOS-based FP (Hamamatsu Photonics K.K., Hamamatsu city, Japan) that contains a 0.15 mm thick CsI:Tl scintillation crystal grown directly on top of the sensor, with an active area of 12×12 cm^2 and pixel size of 0.2, 0.1, or 0.05 depending on the selected binning configuratio (4×4, 2×2, or no binning). Binning also determines the minimum integration time of the detector, which is 0.125, 0.25, and 0.5 s for 4×4, 2×2, and no binning, respectively. Image integration time can be extended up to 10 s regardless of the binning configuration The detector signal is encoded using 12 bits.

To characterize exposure values as a function of energy, we measured x-ray exposure at the isocenter of the scanner using an Accu Gold multi-purpose meter (Radcal, Monrovia, CA) with a 10 cm-long pencil-shaped ion chamber (Radcal 10X6–3CT). Exposure per mAs was measured at 30 and 35 kV and translated to the detector surface by applying the inverse squared distance law.

2.2.2. Estimation of parameters for the detector model. To characterize the gain curve of the detector and its noise level, we acquired series of images for 25 x-ray exposure levels and 4×4 pixel binning for three image integration times: 125, 500, and 1000 ms. Exposure at the detector surface was set by changing the anode current of the tube from zero to above the saturation point of the detector. We acquired 50 images for each exposure level, and, to avoid potential lag effects and instabilities of the x-ray source, the x-ray flu was turned off for 2 s between acquisitions of consecutive series of images. Data were acquired at 35 kVp with no object in the FOV, thus ruling out object-related effects such as beam hardening or scatter. We used a relatively low kVp value for the estimation of the parameters because the DR of the x-ray attenuation values in a sample is larger for low kVps. For this reason low kVps are more appropriate to illustrate the potential offered by our method for increasing the DR of the detector.

Mean signal and variance were computed for each individual pixel in the detector, across the 50 images in each exposure setting.

The overall response of the detector was estimated by averaging the individual values across a 20×20 pixel ROI placed at the center of the detector. The size of the ROI was selected to be large enough to compensate slight deviations between individual pixels but not so much to introduce bias from the x-ray beam shape.

We estimated the dark signal value, p (intercept of the gain curve), as the mean pixel value in absence of radiation, the saturation exposure as the value of exposure where variance departs from its linear trend, and the DR of the pixel signal as the ratio between the saturation exposure and the exposure for a SNR of one (Yaffe 2000). We define the 'quantum limited dynamic range' (DR_Q) as the ratio between the saturation exposure and X_n.

We verifie the validity of the censored Gaussian model for the completion of the linear model for variance at areas near saturation by inspecting the similarity between the theoretical variance from equations (1*b*) and (A.3) and the experimental measurements. The similarity was quantifie as the relative mean absolute error between the measured values

and those predicted by the model, over the dynamic range, according to the following expression

$$\mathrm{RMAE} = \frac{1}{N}\sum_{i=1}^{N}\frac{|v_m(X_i) - v_e(X_i)|}{v_m(X_i)} \tag{5}$$

where v_m is the variance measured experimentally and v_e is the variance estimated using the censored Gaussian model.

To investigate the dependence of the model parameters with integration time we measured the level of dark signal and additive noise for different values of integration time. To this end, we acquired series of 50 dark images for integration times ranging from 0.125 to 2 s and 4 $\times$ 4 binning. Mean value and variance were computed for each pixel and integration time, and the average across all the pixels was assumed to reflec the overall behavior of the detector.

2.3. Assessment of the performance of the HDR method

We used the parameters for the pixel model (see section 2.2.2) to evaluate the potential performance of the HDR method with simulated data. We performed simulations for a generic detector with ideal properties, i.e. limited only by quanta statistics. Details of the simulation process are given in section 2.3.1.

The actual performance of the method was also assessed on realistic small-animal imaging scenarios for both planar (2D) and tomographic (3D) imaging using two dedicated phantoms. Experimental data were acquired using the Argus PET/CT scanner (see section 2.2.1). Each test protocol included the acquisition of a dataset using the dual-exposure technique presented here and a second dataset using a regular single-exposure technique. The number of frames acquired per angular position for the single-exposure data was chosen to match the total exposure used for dual-exposure data, thus making sure that the same dose was delivered to the sample with both protocols.

2.3.1. Theoretical performance of the HDR method for generic ideal detectors. The analysis was carried out for an ideal detector with the h value obtained as described in section 2.2.2, for $p = 0$ and $X_n = 0$ (i.e., no dark signal or instrumentation noise). For this ideal detector, simulations of pixel signal were performed as a function of the attenuation of the x-ray beam. The simulation process consisted in generating a set of pixel values for different pixel exposures, assuming that the pixel signal follows the censored Gaussian distribution described in section 2.1.1.

The air exposure (X_a) (i.e., exposure from the non-attenuated beam) was set to 95% of the saturation exposure, which was obtained as explained in section 2.2.2. The beam was assumed to be attenuated by a range of water thicknesses (x) from 0 to 25 cm at 0.5 cm intervals. According to Beer's law, the pixel exposure for each thickness was calculated as $X_e = X_a \cdot \exp(-\mu_w x)$, where μ_w is the linear attenuation coefficien of water.

We performed 500 realizations of a Gaussian-distributed random variable for each thickness value. We set the mean of the Gaussian function to $m(X_e)$ and variance was given by equations (1*b*) and (A.3). For the sake of simplicity and with no loss of generality, the bit depth of the simulated detector was fi ed to 8 bits, thus yielding 256 possible values for the pixel signal. For the simulation we developed a dedicated routine using Matlab (Mathworks Inc., Natick, MA).

For each water thickness, dual-exposure data were simulated for different values of A_2, from 1 up to $\exp(-\mu_w x)^{-1}$. The simulated signal for each value of A_2 was combined with the original signal (i.e. $A_1 = 1$) using the HDR method, and the SNRs of the combined data were computed.

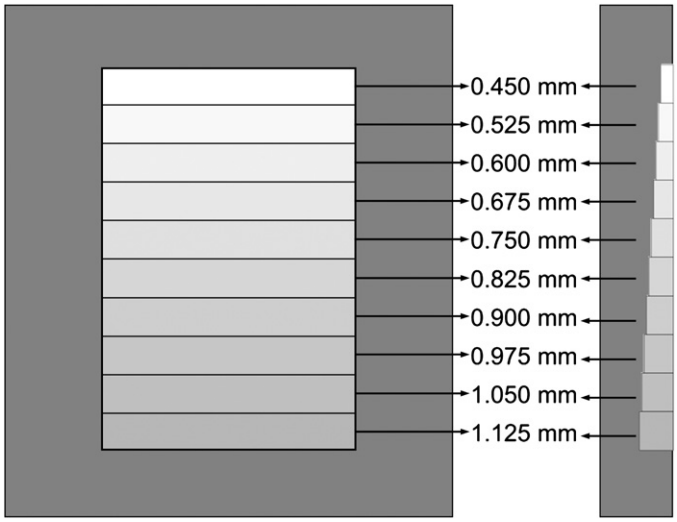

Figure 2. Schematic diagram of the phantom designed to evaluate the performance of the method with 2D projection data. Top (left) and side (right) view. The labels show the thickness of the different copper layers. The lead frame used to block scatter is represented in dark gray.

SNR values obtained with the HDR method were compared to the improvement that would be achieved by averaging an equivalent number of frames encompassing the same total dose to the subject. This improvement factor is the square root of the number of averaged frames, $\sqrt{A_2}$.

Another option for obtaining the dual-exposure dataset could be to increase the image integration time of the detector, instead of the anode current. We also explored the performance of the HDR method with this approach.

2.3.2. Experimental performance evaluation with 2D projection data. We designed and built a dedicated phantom to evaluate the performance of the dual-exposure technique on 2D planar projection data. The phantom consisted of a set of layers of copper tape of different thicknesses ranging from 0.45 to 1.125 mm. The layers were arranged to form a staircase structure as shown in figur 2.

The Argus PET/CT system has a 3 mm thick PMMA tube surrounding the scanner bore to protect the gantry from accidental leakage of fluids When attenuation is very high, the signal can be contaminated by the scatter generated in this protective tube. For this reason, we blocked the portion of the beam non-attenuated by the phantom by framing the phantom in a lead window 2.5 mm thick (see figur 2). This procedure practically suppressed the scattered radiation generated from the protective tube.

To evaluate the performance of the HDR algorithm we measured profile across the staircase pattern and SNR values at each of the steps. SNR values were estimated as the ratio of mean to standard deviation of pixel values, measured on 40 $\times$ 20-pixel ROIs centered on each of the steps.

Table 1 shows the acquisition parameters for the projection data. The dark correction was performed using 50 averaged images. For the gain correction we used 50 averaged images acquired at the nominal current of the single-exposure protocol.

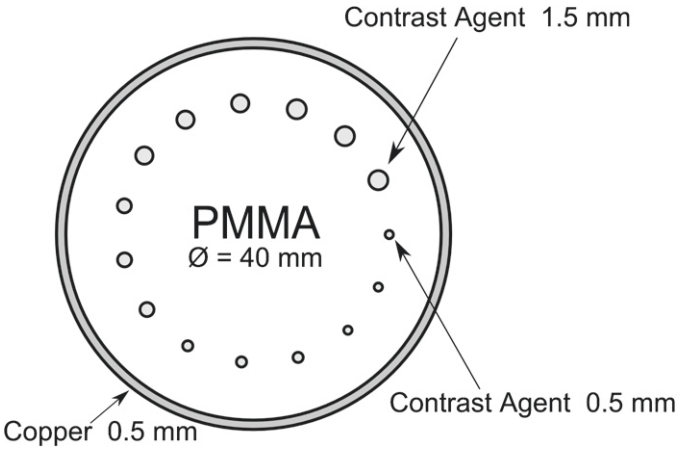

Figure 3. Diagram of the phantom used for estimating contrast resolution. The phantom consists of a uniform PMMA background surrounded by a 0.5 mm thick layer of copper tape. Cylindrical openings of different diameters were drilled on the uniform region and fille with an iodinated contrast agent. The size of the cylindrical inserts ranged from 0.5 to 1.5 mm in 0.25 mm steps, with three inserts per size.

Table 1. Acquisition parameters for projection data.

	Protocol 1		Protocol 2	
Parameter	Dual-exposure	Single-exposure	Dual-exposure	Single-exposure
X-ray beam energy	30 kV	30 kV	35 kV	35 kV
X-ray beam filtratio	1 mm Al	1 mm Al	1 mm Al	1 mm Al
Number of exposures	2	1	2	1
X-ray tube current	0.10/1.00 mA	0.10 mA	0.08/0.96 mA	0.08 mA
Integration time	1500 ms	1500 ms	1000 ms	1000 ms
Frames per projection	1	11	1	13
Total output	1.65 mAs	1.65 mAs	1.04 mAs	1.04 mAs
Acquisition time	3 s	16.5 s	2 s	13 s

2.3.3. Experimental performance evaluation with (3D) tomographic data. Contrast resolution on tomographic slices was evaluated using a dedicated phantom consisting of a homogeneous cylinder of PMMA (density = 1190 kg m^{-3}) with a diameter of 40 mm. The phantom contained cylindrical openings of different sizes that were fille with an iodinated contrast agent (iopamidol 300 mg ml^{-1}, Iopamiro 300, Bracco s.p.a., Milan, Italy). A copper sheet 0.5 mm thick was attached around the PMMA cylinder to simulate a hard bone skull. A sketch of this phantom is shown in figur 3.

As in the previous case, we adjusted the acquisition parameters for the dual- and single-exposure scans to deliver the same radiation dose to the subject under study (see table 2), and the dark and gain corrections were performed as described in section 2.3.2.

Tomographic reconstruction was carried out using a regular FDK approach with a Shepp–Logan windowed ramp filte with cutoff at the Nyquist frequency. Reconstructed volume size was 512 × 512 × 142 voxels with a voxel size of 0.125 × 0.125 × 0.5 mm.

The impact of noise on the detection of the inserts was visually assessed from the images and was also quantitatively evaluated using contrast-to-noise ratio (CNR) measurements. The

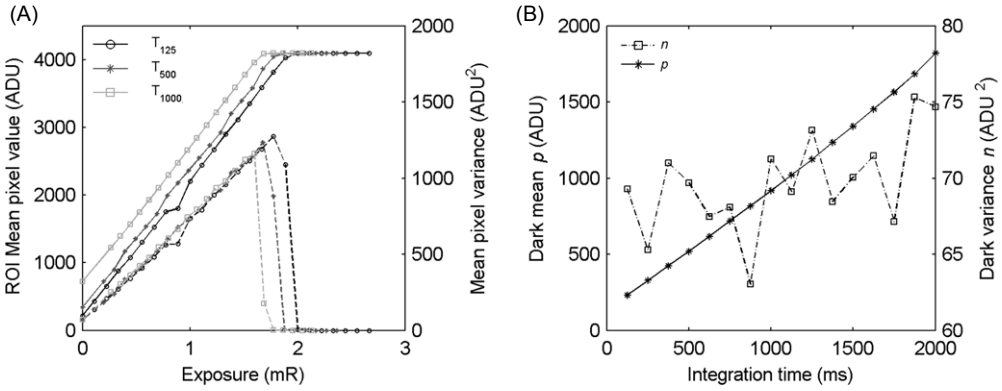

Figure 4. Panel (A) shows the mean pixel signal (solid curves) and variance (dashed curves) as a function of exposure, averaged over the central ROI, and for three image integration times (125, 500 and 1000 ms). Panel (B) shows the mean dark pixel signal p (solid line) and variance n (dashed line), averaged over the same ROI as a function of integration time in absence of radiation.

Table 2. Acquisition parameters for the low-contrast resolution study.

Parameter	Dual-exposure	Single-exposure
X-ray beam peak energy	35 kV	35 kV
X-ray beam filtratio	1 mm Al	1 mm Al
Number of angular projections	360	360
Number of exposures	2	1
X-ray tube current	0.06/0.96 mA	0.06 mA
Integration time	1000 ms	1000 ms
Number of frames per projection	1	17
Total output	367.2 mAs	367.2 mAs
Acquisition time	720 s	6120 s

CNR between the 1.5 mm iodine regions and the PMMA background was measured for both datasets, using the following expression:

$$\mathrm{CNR} = \frac{|\mu_{\mathrm{PMMA}} - \mu_I|}{\sqrt{\sigma^2_{\mathrm{PMMA}} + \sigma^2_I}} \tag{6}$$

where μ_{PMMA} and μ_I are the average voxel value in the PMMA and iodine insert regions respectively, and σ_{PMMA} and σ_I are the standard deviation values inside these regions. The resulting values presented below are the mean of the three CNR values calculated from each of the three 1.5 mm inserts. CNR measurements for inserts smaller than 1.5 mm are not presented since they were subject to a large uncertainty given the small size of the ROI.

3. Results

3.1. Estimation of parameters for the detector model

Figure 4(A) shows the gain curve of the detector and the associated pixel variance as a function of exposure for the three image integration times (125, 500 and 1000 ms) set in the study. Detector pixel variance, averaged over the detector area, shows a linear trend that is broken at the point where some of the pixels enter saturation and the analytical model for variance fails

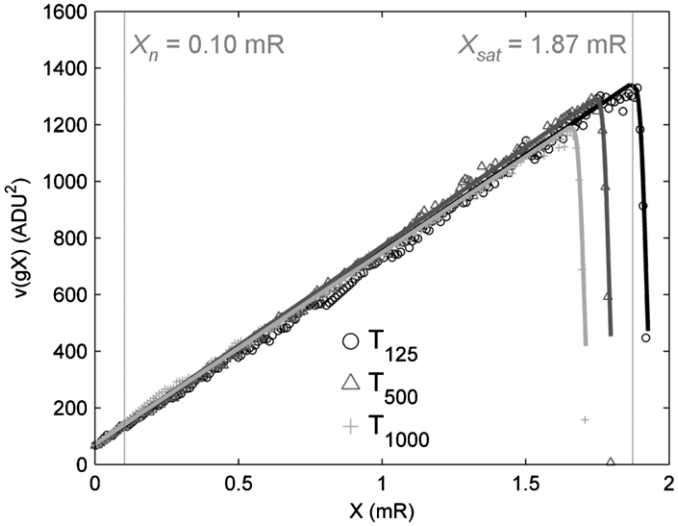

Figure 5. Pixel variance as a function of exposure, after subtraction of the dark signal, shows a linear relationship up to the saturation point of the detector. The theoretical value for pixel variance is shown by solid curves; experimental data are represented by markers.

due to a clipping of the pixel signal. The point where the variance reaches its maximum value was considered the upper limit for the exposure setting.

Variance curves in figur 4(A) show that the extension of the integration time lowers the maximum exposure value. This effect is explained by the increase in dark signal with integration time, shown in figur 4(B). Variance of the dark signal does not seem to depend on integration time, suggesting that X_n is constant across integration time.

The parameters for the linear gain (g) and noise model (X_n and h) extracted from the data in figur 4 were found to be constant across different integration times, showing a constant gain ($g = 2026$ ADU/mR) and level of INEE ($X_n = 0.102$ mR), and a slope relating signal mean and variance of $h = 0.33$. The value of the total instrumentation noise in detector ADUs is therefore $gX_n = 206.7$.

The theoretical variance curve calculated using the censored Gaussian model (see figur 5) shows good agreement with experimental data with relative mean absolute errors of 0.041, 0.032 and 0.039 for integration times of 125, 500 and 1000 ms respectively. The dynamic ranges for unity SNR are DR = 427.18, DR = 398.32, and DR = 378.34, for integration times of 125, 500 and 1000 ms respectively. The dynamic ranges for quantum noise-limited imaging were $DR_Q = 18.73$, $DR_Q = 17.46$, and $DR_Q = 16.59$, for integration times of 125, 500 and 1000 ms respectively.

3.2. Theoretical performance of the HDR method for generic detectors

Results from simulated data are shown in figur 6. When the attenuation of the beam is high enough, the number of photons reaching the detector is not sufficien and frame averaging does not provide any benefi in terms of SNR. This is observed in figur 6(A), when the beam is attenuated by more than 17 cm of water.

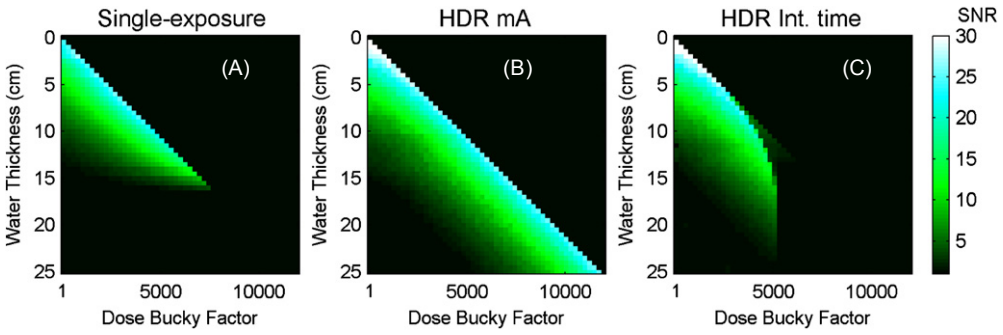

Figure 6. SNR of the acquired data as a function of attenuation and Bucky factor, for frame averaging (A), and for the HDR data obtained by increasing the anode current (B) and the detector integration time (C).

Figure 6(B) shows how the HDR method makes it possible to extend the DR of the acquired data, since the SNR of the data can be maintained constant throughout attenuation by increasing the exposure by the appropriate factor. As opposed to frame averaging, the increase in exposure is translated into a recovery of SNR if the Bucky factor is large enough to provide a valid signal. When the Bucky factor is below that value, the use of the HDR method has the same effect as frame averaging (see lower left corner in figur 6(B)).

When the overexposed dataset for the HDR method is obtained using a longer integration time, the performance of the method suffers a noticeable degradation (see figur 6(C)). The rise of the dark signal narrows the DR of the overexposed image, and cancels out the benefit provided by the HDR method.

3.3. Experimental results on (2D) planar projection data

Figure 7 shows a planar image of the copper pattern phantom, for both the single- and the dual-exposure data, acquired using protocol 1 in table 1 (30 kVp). Both images are displayed after logarithmic transformation of the raw data.

Profil data across the bar pattern for both acquisitions, plotted in figur 8, show how the signal is masked by noise for high attenuation values, thus concealing the transition between consecutive copper thickness values. As expected from the theoretical results above, frame averaging cannot improve SNR in these areas. On the other hand, the steps become visible when the HDR method is applied.

SNR measurements as a function of attenuation in the ROI are shown in figur 9. Using the HDR method, the detector achieved a DR that provides a useful signal for a larger range of attenuation values, while single-exposure data do not provide a valid signal for large thickness values. Note that attenuation factors above $\sim$0.006 are within the quantum noise-limited part of the response curve of the detector when using the HDR method, therefore the DR of the recorded attenuation data is $DR_Q = 166.7$. When using frame averaging the minimum signal above the INEE grows to $\sim$0.013, meaning that the DR is $DR_Q = 76.9$.

3.4. Experimental results on (3D) tomographic data

Figure 10 depicts a slice of the reconstructed volume for the single-exposure and for the dual-exposure scans. The single-exposure image has a poorer contrast resolution, and most of

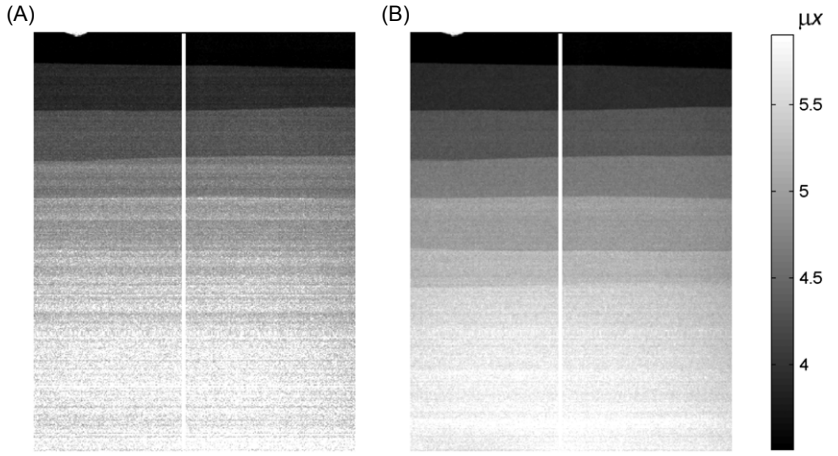

Figure 7. Copper stair phantom acquired using the single-exposure protocol (A) and the dual-exposure protocol (B) for acquisition protocol 1 (30 kVp). The lead frame is not shown on the image. The white line denotes the position where the profil data were measured. The acquisition of both datasets delivered the same radiation dose to the sample.

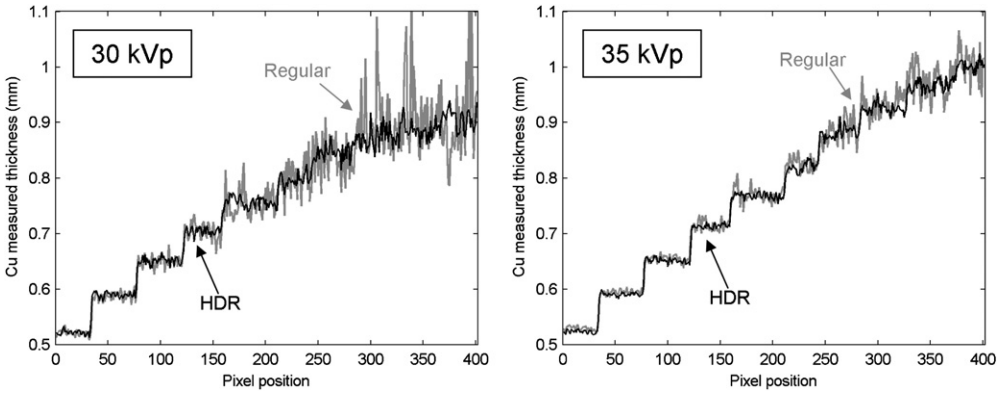

Figure 8. Profil plot across the bar pattern phantom projection for the single-exposure protocol (gray curves) and the dual-exposure protocol (black curves) for 30 kVp (left) and 35 kVp (right), i.e. protocol 1 and 2, respectively (see table 1). Image log values have been normalized by the attenuation factor of copper at the mean energy of the beam to show the estimated thickness of copper. HDR data show a lower noise level for large thickness values, at both energy levels.

the inserts are masked by noise and artifacts (see zoom-in window in figur 10). Using the HDR technique, it is possible to observe a pronounced reduction in the level of ring artifacts and noise present in the data.

The mean CNR value inside the 1.5 mm inserts for the single-exposure data is 0.58, which increases to 1.71 when the HDR method is used.

One of the individual projections used to generate the tomographic data is shown in figur 11, for the different acquisition protocols. Figure 11 shows that a significan part of the pixels (39%) were below the instrumentation noise level (X_n) in the low exposure dataset. On the other hand, these pixels were within the detector quantum noise region in the high current

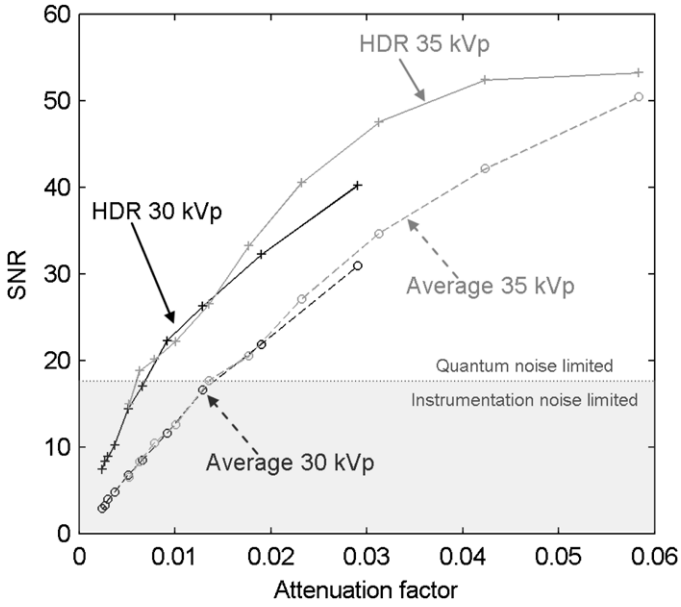

Figure 9. SNR measured inside the ROIs for each of the thicknesses as a function of attenuation factor for the HDR and frame averaged data. The gray shaded area denotes the part of the SNR curves where the instrumentation noise is larger than the quantum noise.

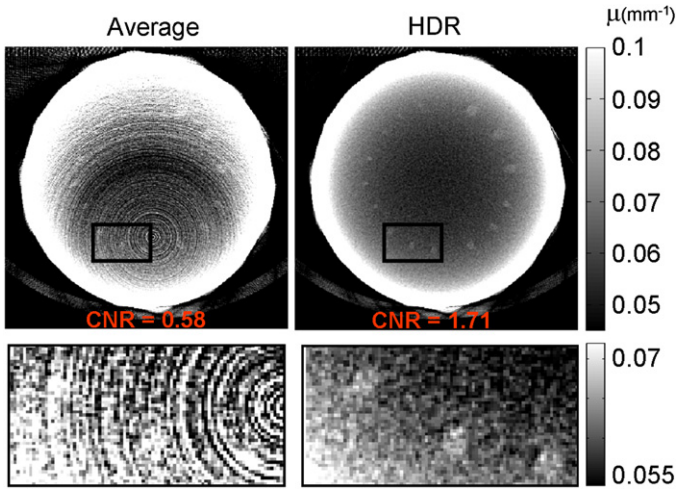

Figure 10. Slice of the contrast resolution phantom acquired using a regular single-exposure protocol (left column) and the dual-exposure protocol developed in this study (right column). The high level of artifacts and noise makes it difficul to discern the inserts from the surrounding background.

dataset. This is reflecte in SNR measurements that show an increase in SNR when using the HDR method, compared to frame averaging, for the same delivered dose. Results for this particular angular position can be extrapolated to any projection due to the symmetry of the phantom.

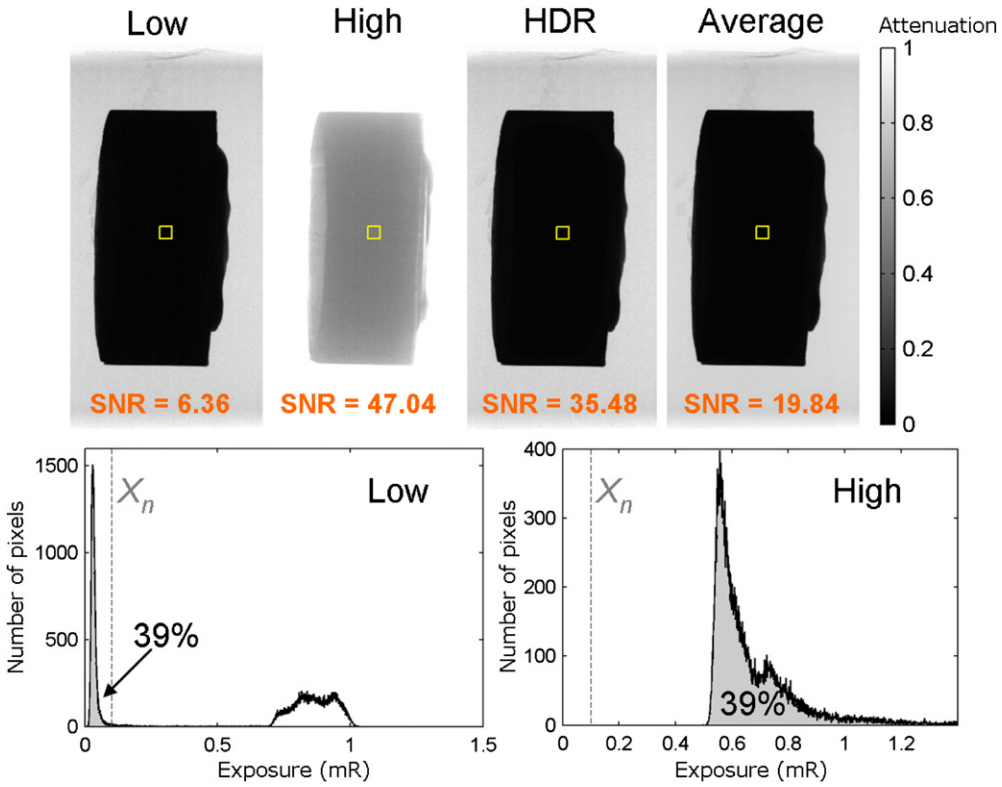

Figure 11. The upper row of the figur shows projection data and associated SNR for one of the projection images used for the CT reconstruction. SNR values were measured for the ROIs marked in the projection images. Note the increase in SNR provided by the HDR method associated with the increase in dynamic range. The bottom row shows the histograms for the low and high current datasets, and the instrumentation noise level. The shaded part of the plot for the low current data shows pixels whose value is below the instrumentation noise level while the shaded part for the high current dataset shows non-saturated pixels.

4. Discussion

The method presented in this study extends the DR of x-ray FP detectors such as those commonly used in CBCT. This extension is achieved by means of a modifie acquisition process and an additional processing stage using the acquired data, thus obviating the need for hardware modification that may be difficul and expensive to implement in commercial devices.

In order to obtain the HDR image, we propose the combination of two datasets using maximum likelihood estimation based on a previously published theoretical model for the mean and variance of pixel signal. The model was extended to take into account the effect of saturation in the variance of pixel signal. The model for detector response showed good agreement with experimental data, thus proving its validity for the realistic simulation of FP detectors.

The detector showed a linear response that broke at the saturation point and a reduction in DR for longer integration times. Since additive noise and variance slope were found to be

constant across integration time, the reduction in DR came solely from the increase in dark signal with integration time.

Simulated data showed that the HDR method could theoretically extend the DR of the detector to infinit , provided that the anode current of the x-ray source could be increased with no limit. A longer integration time reduced the DR of the detector owing to the increase of dark signal. For this reason, the performance of the HDR method degraded when the detector exposure was increased by extending the image integration time instead of the anode current.

Experimental results showed enhanced image quality for projection and tomographic data in samples containing areas of high attenuation. This enhancement resulted from an increase in the DR of the detector and not merely by a reduction of the noise present in the data, as confirme by SNR plots for the same dose delivered to the sample.

The results for the copper staircase phantom showed that the signal inside high attenuation areas was masked by noise in the single-exposure data, due to the lack of a valid signal inside the area in any of the frames acquired. This lack of signal prevented enhancement of the visibility of the phantom structure by frame averaging. After applying the dual-exposure technique, the overexposed image provided a valid signal in some of the highly attenuated areas, revealing the part of the structure that was not visible with the single-exposure data and, therefore, extending the DR of the detector.

Since our method extends the DR of the detected signal, the benefi is larger for highly attenuated areas. This effect is reflecte in the shape of SNR curves for HDR data that show asymptotic behavior for lower attenuation. This result implies the homogenization of the noise properties across high and low attenuation areas, a desirable property for subsequent data processing stages.

With regard to tomographic data, the contrast and noise achieved using the method presented here were better than those obtained using single-exposure methods, when applied to samples containing high attenuation materials that exceed the DR of the detector. The poor contrast resolution in the single-exposure data can be explained by the lack of photons reaching the detector for highly attenuated areas. This lack of photons caused the signal level to be low and more homogeneous in highly attenuated areas. For such low signal values minor deviations in the gain calibration point become much more conspicuous and are the source of the larger impact of ring artifacts. The stronger rings conceal details inside areas surrounded by high attenuation material in the reconstructed volume. Besides the boosting of ring artifacts, low signal levels yielded lower CNR owing to the rise in the relative contribution of additive noise, thus degrading the noise properties of the reconstructed dataset.

Since all the data acquired were used in the combination process, no discontinuities were observed in the reconstructed slices. Discontinuities were observed in previous proposals, which used a simpler approach for the combination of the acquired datasets (Sukovic and Clinthorne 2001).

Our method could be applied to any FP detector, regardless the underlying hardware, provided that the image lag is low enough and does not contaminate the subsequent data frames, especially when a pixel switches from saturation to linear response from one frame to the next. If the time needed to recover from saturation is too large the performance of the method will be reduced. Further work, outside the scope of this paper, would be necessary to assess the maximum level of image lag acceptable to still obtain acceptable results.

We were unable to compare the performance of our method with that of hardware-based approaches, which would certainly be more effective, especially in terms of acquisition time, since only one dataset is acquired. However, our approach is much less expensive and could be included as a minor modificatio to the image processing chain of any system based on an FP detector, regardless of the particular hardware implementation.

Other approaches compensate the limited DR of the detector by pre-equalizing the radiation field assuming prior knowledge of the sample structure. The most widespread technique is the bow-tie filtering which modifie the spatial properties of the beam before it is attenuated by the sample (Mail *et al* 2009) in an attempt to obtain a more even distribution of radiation at the detector surface. When compared with DR extension techniques, such as the one presented here, it is noteworthy that the effect of bow-tie filter is reduced when the acquisition conditions depart from the expected scenario. For instance, if the shape or size of the sample is significantl different from the expected one or there are unexpected high attenuation objects, the DR of the attenuated beam could still be too high for the FP detector. On the other hand, the HDR method presented does not impose any prior condition on the sample properties, offering the same potential for the accommodation of a subject with a larger DR independently of the attenuation distribution of the imaged sample.

The dual-exposure technique proposed here could be further extended to a multi-exposure approach based on several exposure levels to obtain a similar SNR in all the parts of the projection image. However, the maximum mA achievable by the x-ray tube limits the maximum DR that can be obtained using a multi-exposure method.

Future works will involve the study of alternatives to the presented combination algorithm. New models for the probability density functions are also under study.

5. Conclusion

We propose a novel dual-exposure technique to extend the DR of x-ray FP detectors.

Our results show that the method effectively extends the DR of the detector, and increases performance with respect to conventional protocols, particularly when there are high attenuation areas in the sample.

Acknowledgments

This work was funded by the Innovative Medicines Initiative Joint Undertaking under grant agreement no. 115337, which comprises financia contributions from the European Union's Seventh Framework Programme (FP7/2007-2013) and EFPIA companies' in kind contribution. This work was also partially funded by the AMIT project (CEN-20101014) from the CDTI-CENIT program, projects TEC2010-21619-C04-01, TEC2011-28972-C02-01, and PI11/00616 from the Spanish Ministerio de Ciencia e Innovación. AS is funded by an FPU grant from the Spanish Ministerio de Educación.

Appendix

According to the model presented for mean and variance of the pixel signal, the value of a single pixel for a set of acquisitions maintaining a constant radiation flu follows a Gaussian distribution with mean m and variance v given by equation (1*a*). If a significan part of the distribution lies above the maximum pixel signal, all the potential values falling on that part of the curve would receive the maximum pixel value, thus concentrating the upper tail of the distribution in that single value, as shown in figur A.1.

Analytical expressions for mean and variance of Gaussian censored distributions can be found in Greene (2003) and are reproduced below.

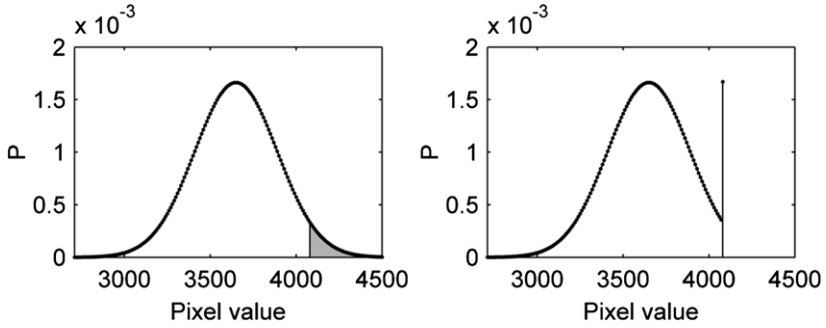

Figure A.1. Probability density function of a Gaussian distribution with $\mu = 3650$ and $\sigma = 240$ representing the distribution of a pixel signal for a 12-bit detector, thus limiting the maximum pixel value to 4095. The plot on the left shows the original distribution of pixel values, while the plot on the right shows the real distribution of pixel values after censoring the upper part (shaded on the left plot).

Let a be the censoring value, i.e., the maximum pixel value, and $m_o(gX)$ and $v_o(gX)$ the mean and variance of the original non-censored distribution, according to equation (1*a*). The mean of the censored pixel distribution is given by

$$m(gX) = (1 - \Phi)a + \Phi\left(m_o(gX) + v_o(gX)^{1/2}\lambda\right), \tag{A.1}$$

where Φ is the cumulative distribution function at point a and λ is given by

$$\lambda = -\frac{\phi(\alpha)}{\Phi(\alpha)}, \quad \text{with} \quad \alpha = \frac{a - m_o(gX)}{v_o(gX)^{1/2}}, \tag{A.2}$$

where ϕ is the probability density function for the non-censored pixel value distribution.

The value for the variance of the censored distribution yields the next expression,

$$v(gX) = v_o(gX)\Phi[(1 - \delta) + (\alpha - \lambda)^2(1 - \Phi)] \tag{A.3}$$

where $\delta = \lambda^2$–$\lambda\alpha$.

References

Badea C T, Johnston S, Johnson B, Lin M, Hedlund L W and Johnson G A 2008 A dual micro-CT system for small animal imaging *Proc. SPIE* **6913** 691342

Boone J M, Nelson T R, Lindfors K K and Seibert J A 2001 Dedicated breast CT: radiation dose and image quality evaluation *Radiology* **221** 657–67

Clinthorne N H and Strobel J 1998 A simple algorithm for restoring images from pixellated radiation detectors *IEEE Nucl. Sci. Symp./Med. Imaging Conf.* vol 2 pp 758–65

Dromigny A and Zhu Y M 1997 Improving the dynamic range of real-time x-ray imaging systems via Bayesian fusion *J. Nondestruct. Eval.* **16** 147–60

Feldkamp L A, Davis L C and Kress J W 1984 Practical cone-beam algorithm *J. Opt. Soc. Am. A* **1** 612–9

Fox T R, Nisius D T, Duncan M Z and Duncan M T 2005 Dynamic range extension of x-ray imaging system used in non-invasive inspection of contraband in vehicles, involves amplifying identical samples of x-ray beams using respective gain values, and forming x-ray image *US Patent* 2005047546-A1; 6901135-B2

Greene W H 2003 *Econometric Analysis* (Upper Saddle River, NJ: Prentice-Hall)

Jaffray D A, Siewerdsen J H, Wong J W and Martinez A A 2002 Flat-panel cone-beam computed tomography for image-guided radiation therapy *Int. J. Radiat. Oncol. Biol. Phys.* **53** 1337–49

Kalender W A and Kyriakou Y 2007 Flat-detector computed tomography (FD-CT) *Eur. Radiol.* **17** 2767–79

Korner M, Weber C H, Wirth S, Pfeifer K J, Reiser M F and Treitl M 2007 Advances in digital radiography: physical principles and system overview *Radiographics* **27** 675–86
Lule T, Schneider B and Bohm M 1999 Design and fabrication of a high-dynamic-range image sensor in TFA technology *IEEE J. Solid-State Circuits* **34** 704–11
Madden B C 1993 Extended intensity range imaging *Technical Report*, *GRASP Lab. University of Pennsylvania* MS-CIS-93-96
Mail N, Moseley D J, Siewerdsen J H and Jaffray D A 2009 The influenc of bowtie filtratio on cone-beam CT image quality *Med. Phys.* **36** 22
Mann S and Picard R W 1995 On being 'undigital' with digital cameras: extending dynamic range by combining differently exposed pictures *Final Program and Proc. Is&T's 48th Annu. Conf.—Imaging on the Information Superhighway* pp 442–8
Nayar S K and Mitsunaga T 2000 High dynamic range imaging: spatially varying pixel exposures *CVPR: IEEE Conf. on Computer Vision and Pattern Recognition (Hilton Head Island, SC)* pp 472–9
Nittoh K, Oyaizu E, Sakurai T, Yoshida T and Mochiki K 2003 Extension of dynamic range in x-ray radiography using multi-color scintillation detector *Nucl. Instrum. Methods Phys. Res.* A **501** 615–22
Robertson M A, Borman S and Stevenson R L 2003 Estimation-theoretic approach to dynamic range enhancement using multiple exposures *J. Electron. Imaging* **12** 219–28
Siewerdsen J H *et al* 2007 Multimode C-arm fluorosco y, tomosynthesis, and cone-beam CT for image-guided interventions: from proof of principle to patient protocols *Proc. SPIE* **6510** 65101A
Siewerdsen J H, Moseley D J, Burch S, Bisland S K, Bogaards A, Wilson B C and Jaffray D A 2005 Volume CT with a flat-pane detector on a mobile, isocentric C-arm: pre-clinical investigation in guidance of minimally invasive surgery *Med. Phys.* **32** 241–54
Sukovic P and Clinthorne N H 2001 A method for extending the dynamic range of fla panel imagers for use in cone beam computed tomography *IEEE Nucl. Sci. Symp./Med. Imaging Conf.* ed J A Seibert (San Diego, CA: IEEE) pp 1647–51
Vaquero J J, Redondo S, Lage E, Abella M, Sisniega A, Tapias G, Montenegro M L S and Desco M 2008 Assessment of a new high-performance small-animal x-ray tomograph *IEEE Trans. Nucl. Sci.* **55** 898–905
Whiting B R, Massoumzadeh P, Earl O A, O'Sullivan J A, Snyder D L and Williamson J F 2006 Properties of preprocessed sinogram data in x-ray computed tomography *Med. Phys.* **33** 3290–303
Yadava G K, Kuhls-Gilcrist A T, Rudin S, Patel V K, Hoffmann K R and Bednarek D R 2008 A practical exposure-equivalent metric for instrumentation noise in x-ray imaging systems *Phys. Med. Biol.* **53** 5107–21
Yaffe M J 2000 *Handbook of Medical Imaging Physics and Psychophysics* vol 1 ed H L Kundel, J Beutel and R L van Metter (Bellingham, WA: SPIE Optical Engineering Press)
Yang K, Huang S Y, Packard N J and Boone J M 2010 Noise variance analysis using a fla panel x-ray detector: a method for additive noise assessment with application to breast CT applications *Med. Phys.* **37** 3527–37
Yu L F, Zou Y, Sidky E Y, Pelizzari C A, Munro P and Pan X C 2006 Region of interest reconstruction from truncated data in circular cone-beam CT *IEEE Trans. Med. Imaging* **25** 869–81
Zbijewski W *et al* 2011 A dedicated cone-beam CT system for musculoskeletal extremities imaging: design, optimization, and initial performance characterization *Med. Phys.* **38** 4700–13